Supplementary Information (SI) for ChemComm.

Electronic Supplementary Information

Scale-up Synthesis of Amorphous Ni-Fe Tungstate for Highly-Efficient Oxygen Evolution Reaction

Heng Chen,‡ [a] Xinyue Yang,‡ [a] Yueli Wang,‡ [a] Gaoyan Zhang,[b] Nairui Luan,[a] Qingcheng Zhang,* [a] Fan He,[a] Siting Lv,[a] Xi Yu,[a] Xijun Liu,[c] Wei Zhang,* [d] Ge Meng,* [a] Yong Lei,* [e] and Shun Wang* [a]

[a]College of Chemistry and Materials Engineering, Key Laboratory of Leather of Zhejiang Province, Wenzhou University, Zhejiang 325035, China.

E-mail: zhangqc@wzu.edu.cn (Qingcheng Zhang), mengge@wzu.edu.cn (Ge Meng), shunwang@wzu.edu.cn (Shun Wang)

[b]Technology Institute of Wenzhou University in Yueqing, Wenzhou 325099, China

[c]State Key Laboratory of Featured Metal Materials and Life-cycle Safety for Composite Structures, Guangxi Key Laboratory of Processing for Non-ferrous Metals and Featured Materials, School of Chemistry and Chemical Engineering, Guangxi University, Nanning, 530004 Guangxi, China.

[d]College of Electrical Engineering, Zhejiang University of Water Resources and Electronic Power, Hangzhou 310018, China.

E-mail: zhangw@zjweu.edu.cn (Wei Zhang)

[e]Fachgebiet Angewante Nanophysik, Technische Universität Ilmenau, Ilmenau 98693, Germany.

E-mail: yong.lei@tu-ilmenau.de (Yong Lei)

‡ These authors contributed equally.

Experimental Section

Materials: Potassium hydroxide (KOH), anhydrous ethanol [C_2H_5OH;⩾99.5%], iron nitrate nonahydrate [$Fe(NO_3)_3\cdot 9H_2O$, 98%], nickel nitrate hexahydrate [$Ni(NO_3)_2\cdot 6H_2O$; 98%], sodium tungstate dehydrate [$Na_2WO_4\cdot 2H_2O$, 99.5%], and Nafion solution [$C_{10}H_8O$; 5 wt.%] were purchased from Aladdin Chemical Reagent Co. Ltd. Ruthenium dioxide [RuO_2; ⩾99.99%] catalyst was provided by Alfa Aesar (China) Chemical Co. Ltd. All chemicals were used directly without additional purification.

Synthesis of Ni-Fe Tungstate: $NiFeWO_4$-3 was synthesized using a co-precipitation process in MISR (its geometrical structure can be seen in Ref.[1] Typically, 0.5 mol L^{-1} of $NiCl_2$ and $FeCl_3$ mixed solution (molar ratio $Ni^{2+}/Fe^{3+}=3$) and 0.5 mol L^{-1} Na_2WO_4 were simultaneously pumped into MISR at the volumetric flow rates of 100 mL min^{-1} for high-speed impact. The precipitates were formed immediately and flowed into a beaker for vigorously stirring for 1h. Subsequently, the precipitates were quickly placed in liquid nitrogen to freeze completely. Then, the precipitates were washed in a centrifuge six times, alternately using deionized water and absolute ethanol to remove the residual NaCl. Finally, the moist product was dried at 60°C for 12h and ground to a yellow powder, which was then annealed at 260°C for 2h to obtain $NiFeWO_4$-3.

The effects of Ni^{2+}/Fe^{3+} ratio, reactant concentration and flow rate on the structure and properties of the $NiFeWO_4$ materials were also studied. All the $NiFeWO_4$ materials were synthesized in MISR with the same procedure of $NiFeWO_4$-3, with only a single variable being altered. Firstly, $NiFeWO_4$ materials with different Ni^{2+}/Fe^{3+} ratios were synthesized in MISR, the obtained samples with Ni^{2+}/Fe^{3+} ratios of 2:1 and 10:1 were denoted as "$NiFeWO_4$-2" and "$NiFeWO_4$-10", respectively. Secondly, $NiFeWO_4$ materials were synthesized with different concentrations of metal chlorides solutions (i.e., C_m = 0.1, 0.5 and 1.0 mol L^{-1}), while the molar concentration ratio of metal chlorides to Na_2WO_4 solution was kept at 1. Finally, $NiFeWO_4$ materials were synthesized at different volumetric flow rates. The volumetric flow ratio of the two streams was kept at 1, with varying volumetric flow rates (V_A) ranging from 50 to 150 mL min^{-1}.

For comparison, $NiWO_4$ and $FeWO_4$ were also synthesized in MISR with the same procedure of $NiFeWO_4$-3, except that Ni^{2+}/Fe^{3+} mixed solution was replaced by 0.5 mol L^{-1} $NiCl_2$ and 0.5 mol L^{-1} $FeCl_3$, respectively.

*Synthesis of NiFeO-3:*0.5 mol L^{-1} $NiCl_2/FeCl_3$ solution (Ni^{2+}/Fe^{3+}=3:1) was also precipitated with 1 mol L^{-1} NaOH solution in MISR by the same strategy as the $NiFeWO_4$-3. Afterwards, the precursor was annealed at 260℃ for 2h to obtain NiFeO-3.

Characterization

The morphological characteristics of the synthesized catalysts were observed with scanning electron microscopy (SEM; Hitachi, S-4800, 15 kV) and transmission electron microscopy (TEM; JEOL, JEM-2100F, 200 kV). High-resolution transmission electron microscopy analysis, X-ray energy dispersive spectrometer (EDS), and selected area electron diffraction (SAED) were also performed on the JEM-2100F microscopy. The physical phases of the catalysts were measured by X-ray diffractometer (XRD, Bruker D8) with Cu Kα radiation (λ=1.5418 Å), and the patterns were recorded within 2θ ranging from 20° to 80° at a scan rate of 2° min^{-1}. X-ray photoelectron spectroscopy (XPS) was analyzed using a Thermo Scientific EscaLab 250Xi equipped with an Ar^+ sputter ion gun. The chemical states and molecular structures of elements were measured by bombarding the sample on Ti foil with Ar^+ (accelerated to 1 keV) as the exciting source. The spectral data were analyzed and fitted with Avantage software. The N_2 adsorption/desorption isotherms of catalysts were conducted on a Micromeritics apparatus (ASAP 2020M), while their specific surface areas (SSAs) and pore size distributions were calculated with the Brunauer-Emmett-Teller method. The contents of Ni, Fe, W, and O were analyzed on inductively coupled plasma optical emission spectrometry (ICP-OES) with PE Optima 8000. Fourier transform infrared (FTIR) spectra were recorded in the range of 4000-400 cm^{-1} using a TRENSOR 27 spectrometer. Raman spectra were measured by a laser micro-Raman spectrometer (invia) equipped with an excitation wavelength of 532 nm.

The electrocatalytic measurements were conducted on CHI760E (Shanghai Chenhua Instruments Co., Ltd., China) in a conventional three-electrode configuration using 1.0 M KOH as the electrolyte. The as-prepared catalysts attached to glassy carbon (GC, 5 mm diameter, 0.196 cm^{-2}) were served as working electrodes, Pt plate and Hg/HgO (1.0 M KOH) were employed as the counter electrode and reference electrode, respectively. The catalyst ink was prepared by dispersing 5 mg catalyst into 960 μL ethanol and 40 μL Nafion (5 wt %) solution, which was then ultrasonic treated for 30 minutes to obtain homogeneous ink. Subsequently, 10 μL dispersion was dipped and dried onto the GC disk at room temperature for 10 min. All electrode potentials were converted with respect to the reversible hydrogen electrode (RHE) according to the equation ($E_{RHE}=E_{(Hg/HgO)}+0.098+0.0591$ pH). The current density was calculated from the ratio of the current value at the catalyst surface to the geometric area of electrolyte contact. Prior to the electrochemical measurements, the working electrode was polished with alumina powder to ensure the accuracy of subsequent measurements. The cyclic voltammograms (CV) curves were recorded at the scan rate of 100 mVs^{-1} within the potential range of 0-1 V. The polarization curves towards the catalyst electrode were measured by linear sweep voltammetry (LSV) with a sweep rate of 5 mV s^{-1} and 90% automatic compensation within 0-0.7 V. The overpotential (η) was obtained from the LSV curve and calculated using the relationship: $\eta=E_{(RHE)}-1.23$. In addition, the Tafel slope (b) was calculated from LSV results according to the Tafel equation: ($\eta= b \log j+a$), where η, j, and a represented the overpotential, current density, and constant value, respectively. Electrochemical impedance spectroscopy (EIS) measurements were conducted within the 0.01-100 kHz frequency range. The electrochemical active surface area (ECSA) of electrode materials was determined with CV curves in 0.326-0.426 V at scan rates of 40–120 mV s^{-1}, which could be calculated from the double-layer capacitance based on the equation ($ECSA=C_{dl}/Cs$), where the specific capacitance (C_S=0.040 mF cm^{-2}) is acquired according to typical reported values. The stability test was assessed by CV measurements for 2000 cycles and the i-t curve for 160h. The overall water-splitting performances were measured using $NiFeWO_4$-3 as the cathode and commercial Pt/C as the anode in a typical two-electrode configuration (1.0 M

KOH). The CV profiles were recorded in 1.2-2 V at a scan rate of 50 mV s^{-1}, while a scan rate of 5 mV s^{-1} and a potential window of 1.2-2 V were chosen for the polarisation curve. The stability was assessed by the i-t curve for 110h. The polarization curves of cataysts evaluated at 25°C to 55°C are depicted to calculate the activation energy required for OER. The activation energies (E_a) of $NiFeWO_4$-3 and NiFeO-3 catalysts are calculated by plotting a geometric function of ln(j) versus 1/T.

DFT Calculations

All simulations were conducted on the Vienna Ab initio Simulation Package (VASP) based on the periodic spin-polarized density functional theory (DFT).[2-4] The ion-core interactions were described using the Projected Augmented Wave (PAW) method,[5] and the exchange-correlation effects were accounted for using the Perdew-Burke-Ernzerh (PBE) functional within the generalized gradient approximation (GGA).[6] The Brillouin zone of the $NiFeWO_4$-3 (NiFeO-3) surface was sampled using a 2×1×1 (2×2×1) Monkhorst-Pack K-point mesh, and the plane wave basis set had a cutoff energy of 450 (550) eV. Convergence criterions of 10^{-5} eV and 0.02 eV/$Å^{-2}$ were set to electronic iterations and atomic forces, respectively. The calculation parameters had been shown an accurate description of the geometry structures of bulk $NiWO_4$ (lattice constants: a=4.6 Å, a=5.69 Å, c=4.95 Å) and bulk NiO (lattice constants: a=b=c=4.15 Å), which consisted well with experimental values ($NiWO_4$: a=4.6 Å, a=5.66 Å, c=4.91 Å; NiO: a=b=c=4.15 Å).[7, 8] The surface of $NiFeWO_4$-3 catalyst was constructed by averagely replacing the bottom and top Ni atoms with Fe atoms in a 2×1×1 $NiWO_4$ (010) supercell (contains 8 oxygen layers), resulting in $Fe_2Ni_6W_8O_{32}$. Similarly, NiFeO-3 was built by replacing the bottom and top Ni atoms with Fe atoms in a 2×2×1 NiO (001) supercell (contains 4 atomic layers), which could be expressed as $Fe_2Ni_{30}O_{32}$. The central 2 oxygen layers of $NiFeWO_4$-3 and central 2 atomic layers of NiFeO-3 were fixed during simulations. A vacuum region of 20 Å was included between slabs to prevent interactions between periodic cells. The surface energy of clean $NiWO_4$ (010) was calculated to be 0.48 J/m^2, which was close to the reported 0.62 J/m^2. [9] The predicted surface energy of clean NiO (001) was 1.27 J/m^2, agreed well with other predictions

(1.15 J/m^2).[10] Implicit solvent of water was considered using Polarizable Continuum Model (PCM) as implemented in VASPsol due to the significant impact of dispersion on adsorption predictions.[11] For the solvent parameters, the dielectric constant ε_r, surface tension of cavity τ and the cutoff charge density n_c were set to 78.4, 0 meV/Å^{-2} and 2.5 ×10^{-4} Å^{-3}, respectively. The free energy was estimated by correcting the ground-state DFT energies with zero-point energies and entropies at pH=0, U=0 V/NHE and T= 300K.

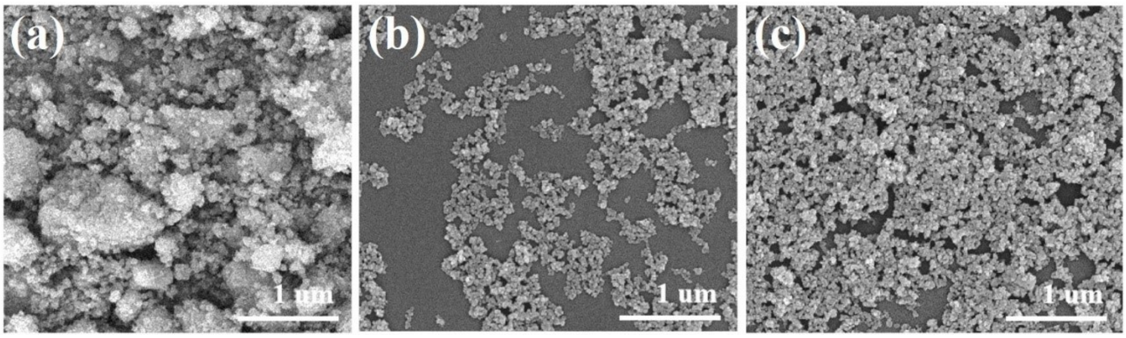

Fig. S1. (a)-(c) SEM images of the NiFeWO$_4$ materials synthesized at the volumetric flow rates of 50, 100 and 150 mL min^{-1}, respectively.

When the volumetric flow rate is increased from 50 to 100 mL min^{-1}, the aggregated NiFeWO$_4$ particles become smaller and more uniform with sizes range from 30-40 nm (Fig. S1a-b). Our previous studies have found that in the range of low volumetric flow rate, the impinging of two reactant streams may not be developed completely and the micromixing efficiency in MISR is relatively low.[12] The turbulent kinetic energy in MISR will be intensified with the increasing flow rate to enhance the micromixing performance between the two fluid flows, hence the co-precipitation of NiFeWO$_4$ particles can be conducted in the homogeneous supersaturation environment. As a consequence, the generated NiFeWO$_4$ particles become smaller and the aggregation phenomenon is greatly weakened. In addition, the micromixing efficiency of MISR will reach a constant platform after the impinging zone gets fully developed with further increasing volumetric flow rates, hence no noticeable changes to the morphology of NiFeWO$_4$ materials are observed when the volumetric flow rate is further increased from 100 to 150 mL min^{-1} (Fig. S1c). It is well known that reducing the particle size results in more exposed active sites and the enhanced electroactivity, hence the $NiFeWO_4$ materials synthesized at high volumetric flow rates (100 and 150 mL min^{-1}) are expected to display higher OER performances than that synthesized at 50 mL min^{-1}.

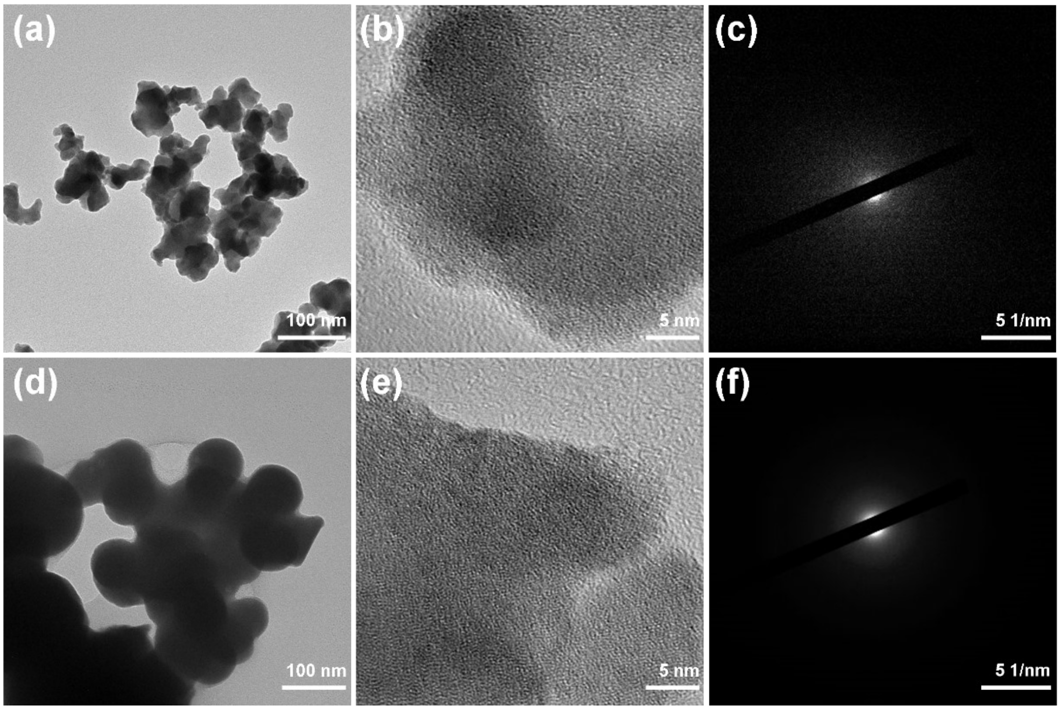

Fig. S2. TEM, HRTEM and SAED images of (a-c) $NiWO_4$. (d-f) $FeWO_4$.

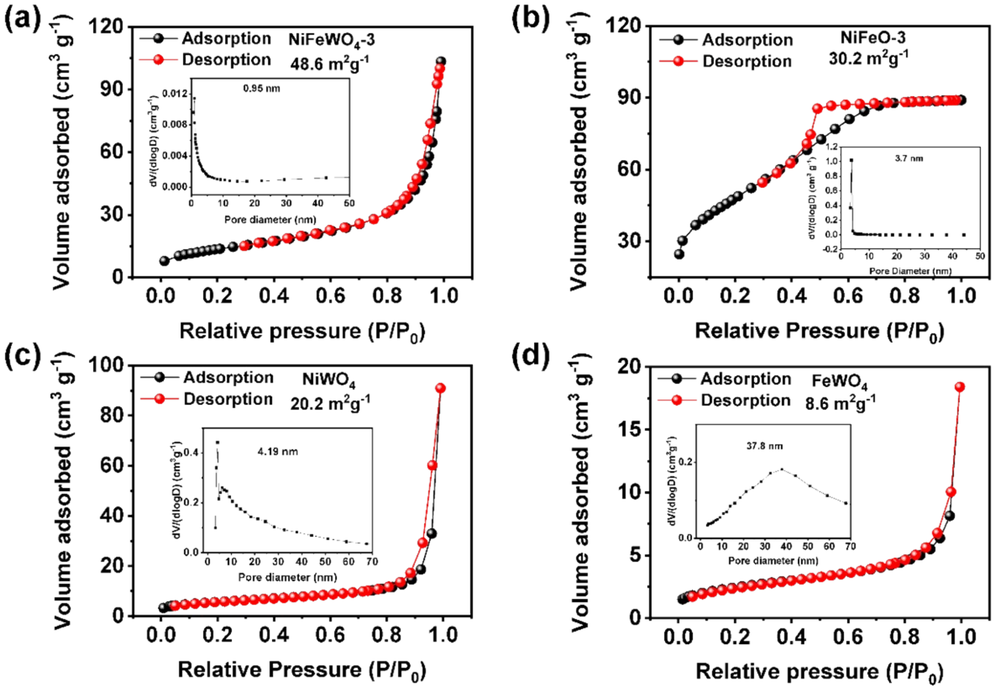

Fig. S3. BET specific surface area and pore size distribution of (a) $NiFeWO_4$-3. (b) $NiFeO_4$-3. (c) $NiWO_4$. (d) $FeWO_4$

The specific surface area (SSA) and pore size distribution (PSD) are key factors in determining OER performance. As shown in Fig. S3, the SSA of NiFeWO$_4$-3 (48.6 m^2 g^{-1}) is much larger than those of NiFeO-3 (30.2 m^2 g^{-1}), NiWO$_4$ (20.2 m^2 g^{-1}) and FeWO$_4$ (8.6 m^2 g^{-1}). Apart from FeWO$_4$, other catalysts display microporous structures with PSD range of 1~5 nm, which are derived from the internal pores within the nanoparticles or loose aggregates. Higher SSA and suitable microstructure can provide more active sites and unhindered diffusion pathways for electrolyte ions to participate in OER process, thereby greatly contributing to their catalytic activities.

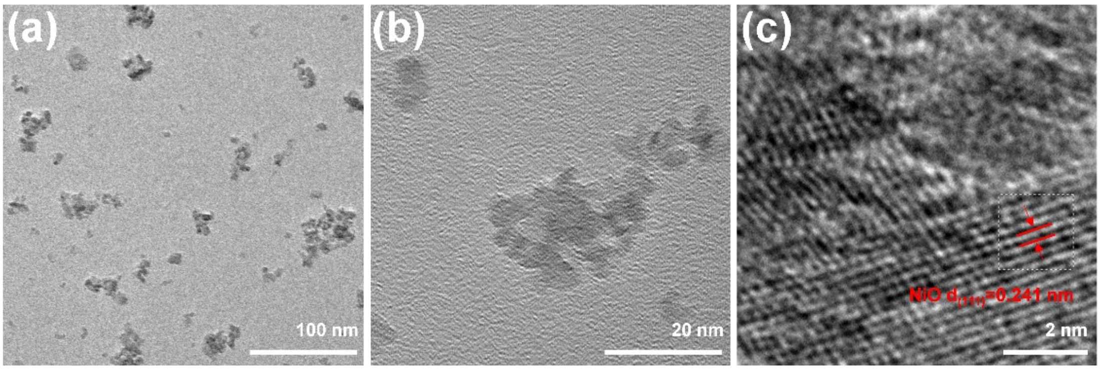

Fig. S4. (a, b) TEM images; (c) HRTEM image of NiFeO-3.

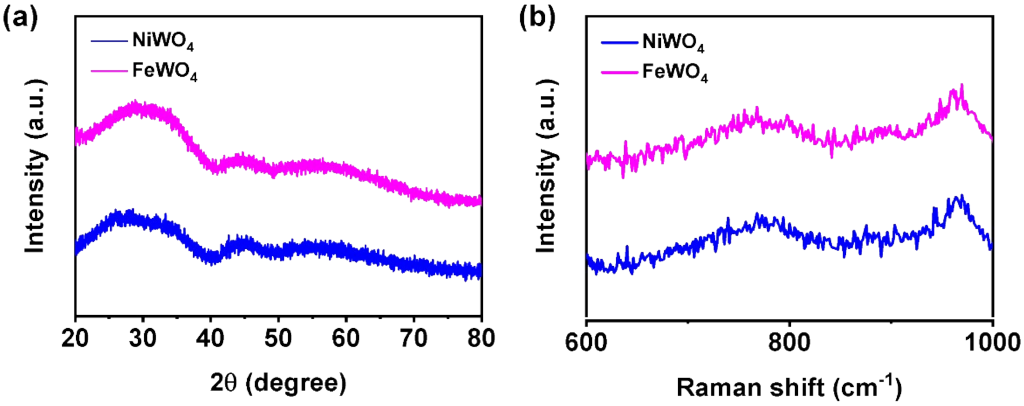

Fig. S5. (a) XRD patterns of NiWO$_4$ and FeWO$_4$. (b) Raman spectra of NiWO$_4$ and FeWO$_4$.

The Raman spectra of NiFe-based tungstates and oxide are shown in Fig. 2b and Fig. S5b. NiFe-based tungstates show a peak of 771 cm^{-1} that can be assigned to the asymmetric stretching of W=O, while the main peak at 950 cm^{-1} is derived from the valence vibration of surface W=O.[13] In contrast, NiFeO-3 shows two main peaks at 557 and 675 cm^{-1}, which can be ascribed to the one-phonon LO modes and two-phonon

2TO modes of NiO, respectively.[14, 15]

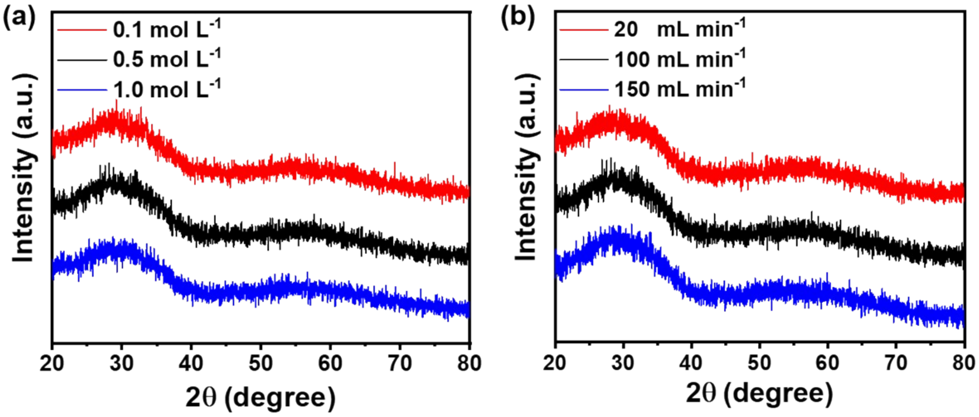

Fig. S6. (a) XRD patterns of NiFeWO$_4$ materials synthesized with different reactant concentrations; (b) XRD patterns of NiFeWO$_4$ materials synthesized at different volumetric flow rates.

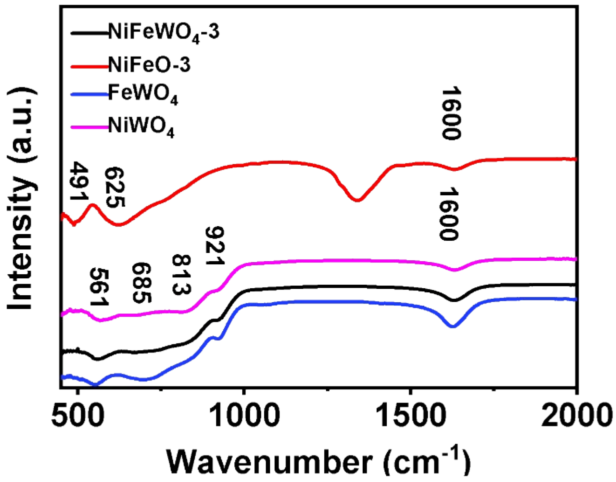

Fig. S7. Fourier-transform infrared spectra of NiFeWO$_4$-3, NiWO$_4$, FeWO$_4$. and NiFeO-3.

The FT-IR spectra of NiFe-based tungstates and oxide are shown in Fig. S7. the characteristic peak at 921 cm^{-1} is classified as the valence vibration of surface W=O, while the peaks at 813 cm^{-1} and 683 cm^{-1} are derived from the stretching vibration mode of W-O-W. In addition, the absorption bands at 1600 cm^{-1} and 567 cm^{-1} are associated with the bending modes of the -OH group and the bending vibration of Fe-O, respectively.[16, 17] Meanwhile, the FT-IR spectrum of NiFeO-3 exhibits the adsorption bands at 490 cm^{-1}, 625 cm^{-1}, and 1600 cm^{-1} that can be assigned to the Ni–O, Fe–O stretching mode,[18] and adsorbed water, respectively.

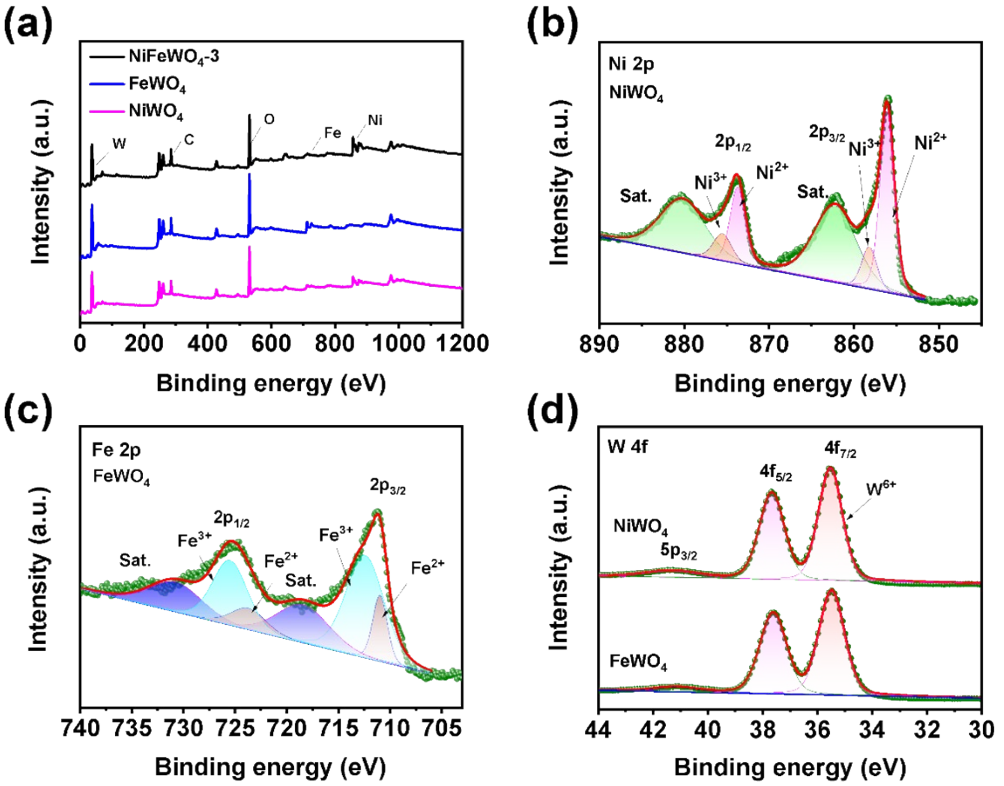

Fig. S8. (a) XPS survey of NiFeWO$_4$-3, NiWO$_4$, and FeWO$_4$. (b) Ni 2p XPS of NiWO$_4$. (c) Fe 2p XPS of FeWO$_4$. (d) W 4f XPS of NiWO$_4$ and FeWO$_4$.

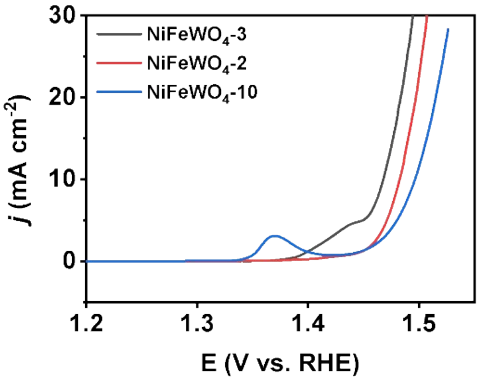

Fig. S9. The polarization curves of NiFeWO$_4$-3, NiFeWO$_4$-2, and NiFeWO$_4$-10 loaded on glassy carbon in 1M KOH with iR-corrected. Scan rate: 5 mV s^{-1}

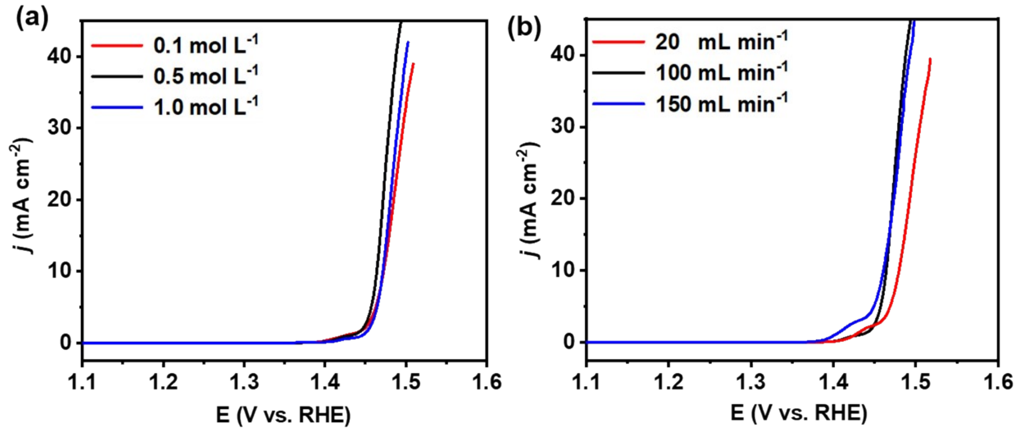

Fig. S10. (a) LSV curves of $NiFeWO_4$ materials synthesized with different reactant concentrations; (b) LSV curves of $NiFeWO_4$ materials synthesized at different volumetric flow rates.

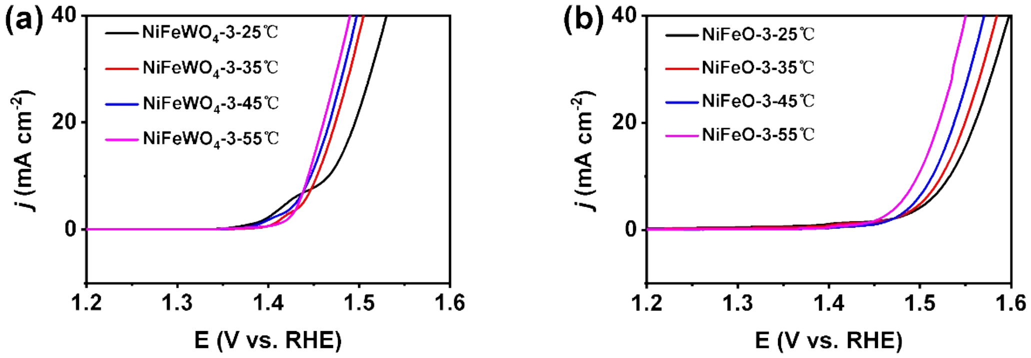

Fig. S11. OER polarisation curves tested at different temperatures (25℃, 35℃, 45℃, and 55℃) in 1.0 M KOH. Scan rate: 5 mV s^{-1} (a) $NiFeWO_4$-3. (b) NiFeO-3.

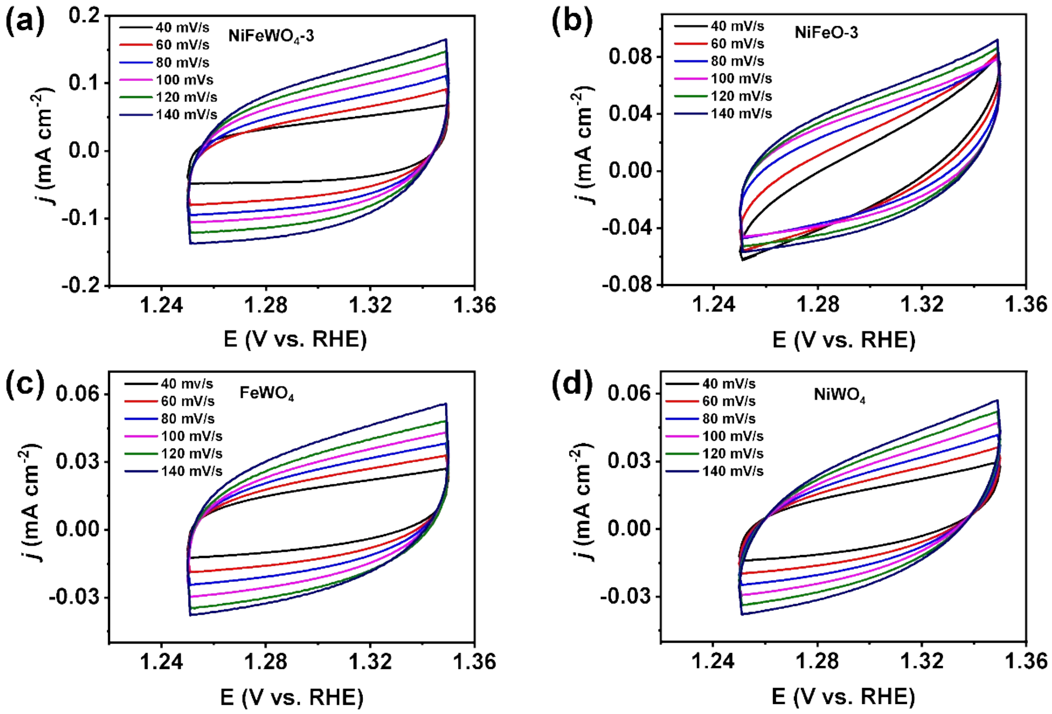

Fig. S12. CV curves in the range 1.25~1.35 V (RHE) for various samples. (a) NiFeWO$_4$-3. (b) NiFeO-3. (c) FeWO$_4$. (d) NiWO$_4$. Scan rate: from 40 to 140 mV s^{-1}.

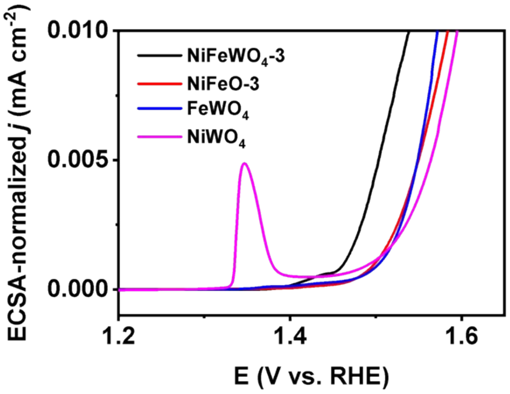

Fig. S13. ECSA-normalized LSV curves for NiFeWO$_4$-3, NiFeO-3, FeWO$_4$, and NiWO$_4$.

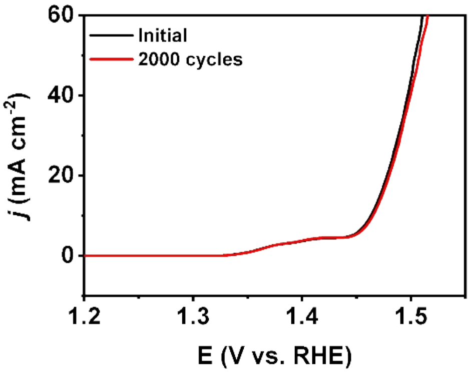

Fig. S14. LSV curves of NiFeWO$_4$-3 catalyst before and after 2000 CV cycles.

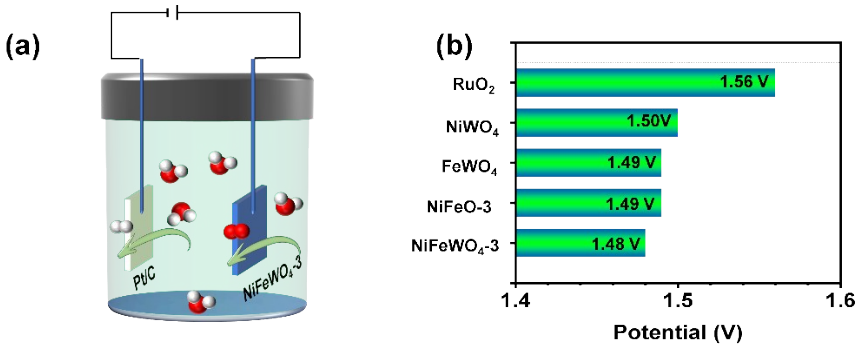

Fig. S15. (a) Schematic diagram of over water splitting. (b) Overall water splitting voltage at a current density of 10 mA cm^{-2}.

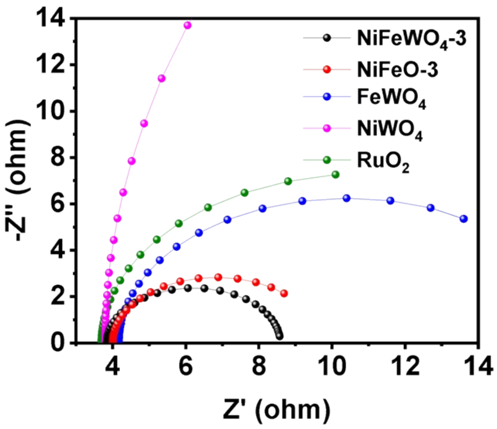

Fig. S16. EIS Nyquist plots toward overall water splitting.

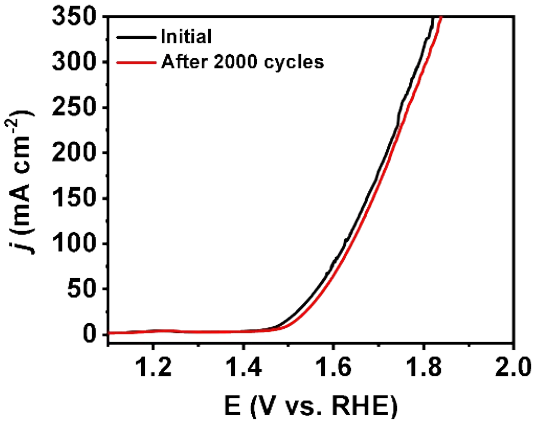

Fig. S17. LSV curves of NiFeWO$_4$-3 catalyst before and after 2000 CV cycles toward overall water splitting.

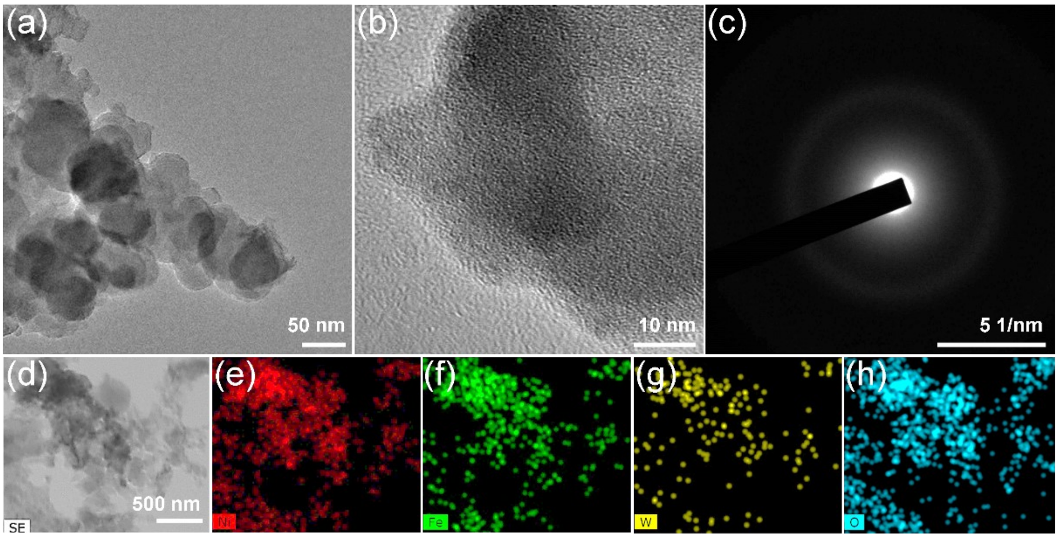

Fig. S18. (a) TEM of NiFeWO$_4$-3 catalyst after 110 h of continuous OER in three-electrode configuration. (b) HRTEM image. (c) SAED pattern. (d) EDS elemental mapping images of Ni (e), Fe (f), O (g), and W (h).

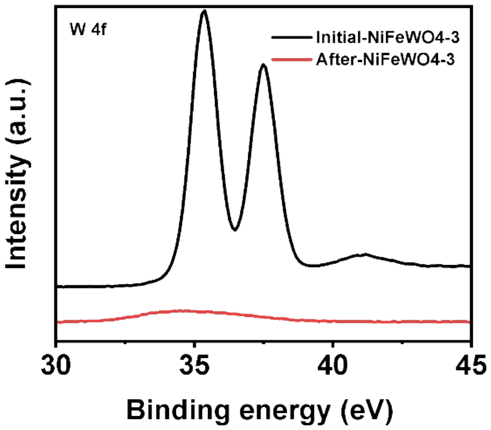

Fig. S19. XPS spectra before and after OER process of W 4f in three-electrode configuration.

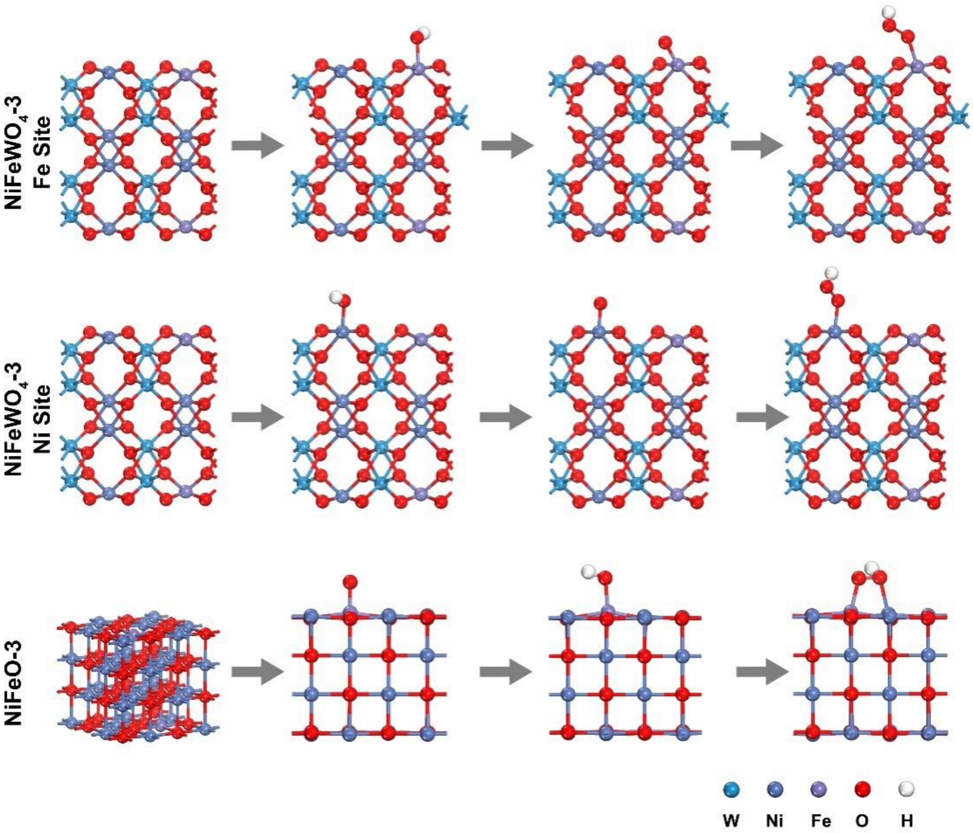

Fig. S20. Optimized crystal structures for OER process over NiFeWO$_4$-3—Fe sites, F NiFeWO$_4$-3—Ni sites and NiFeO-3 following the corresponding reaction steps.

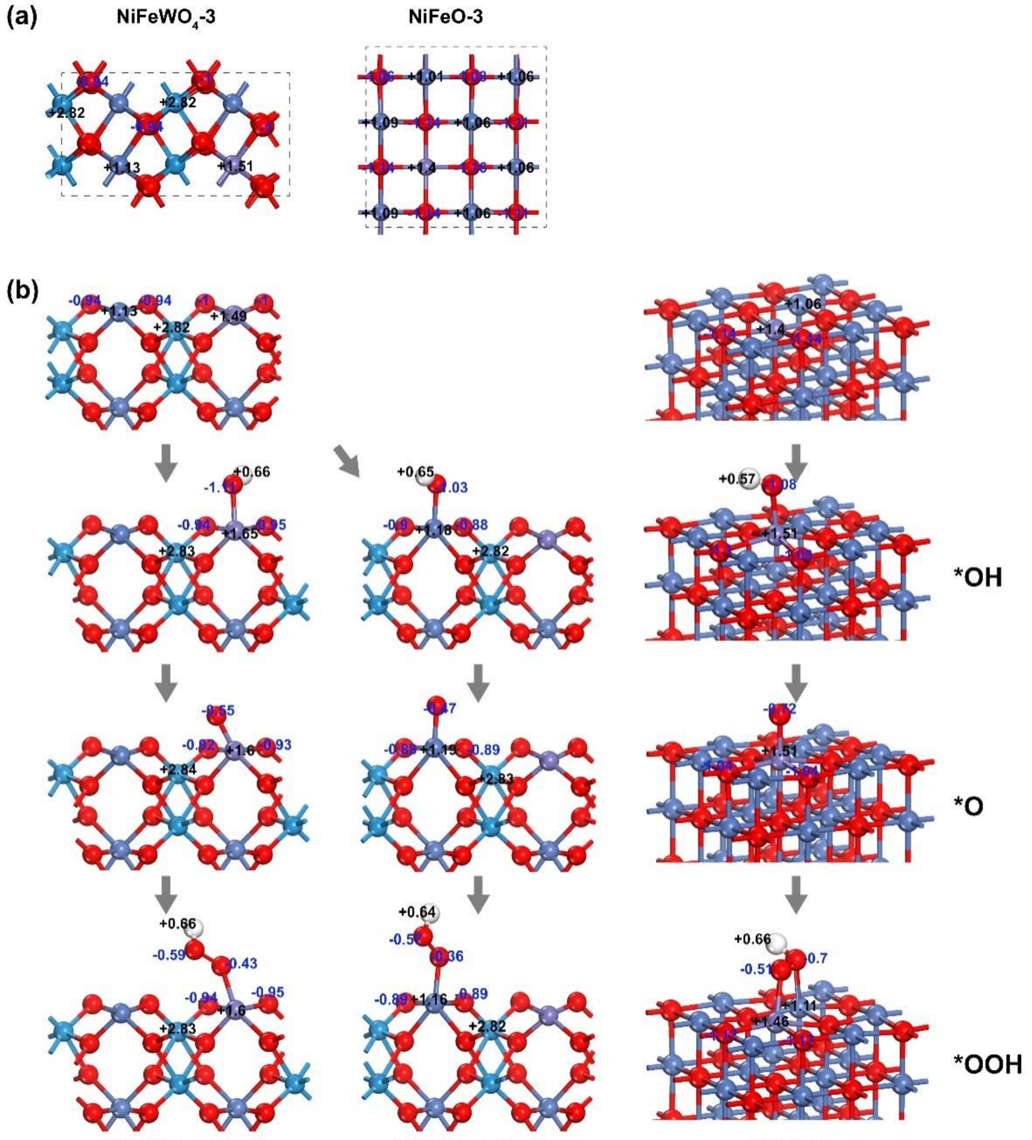

NiFeWO$_4$-3-Fe site **NiFeWO$_4$-3-Ni site** **NiFeO-3**

Fig. S21. Bader charge analysis for OER process over NiFeWO$_4$-3—Fe sites, NiFeWO$_4$-3—Ni sites, and NiFeO-3 surface.

Table S1. Comparison of catalytic performances of previously reported OER catalysts attached glassy carbon.

Catalysts	η (mV) @ (mA cm^{-2})	Tafel slope (mV dec^{-1})	Durability	References
NiFeW	248 @ 20	68.0	6 h at 50 mA cm^{-2}	19
Ni_2Fe_1@PANI	240 @ 20	82	60000 s at 1.47 V	20
$Ni_{60}Fe_{40}$-S/NSC	239@ 10	30.9	30000 s at 10 mA cm^{-2}	21
FeCoMo-Se	264@ 10	33.0	100 h at 10 mA cm^{-2}	22
Co@NiFe-LDH	253 @ 20	44.0	50 h at 10 mA cm^{-2}	23
$Co_xFe_{1-x}P$	277 @ 10	37.0	40000 s at 10 mA cm^{-2}	24
FeCoNiPB	235 @ 10	53	41 h at 10 mA cm^{-2}	25
NiFe-ANR	228 @ 10	37	10 h at 10 mA cm^{-2}	26

a/c-$NiFeMoO_x$	256 @ 10	41.7	50000 s at 10 mA cm^{-2}	27
Fe_4Co_6@NDC	307 @ 10	55	112 h at 10 mA cm^{-2}	28
F-Co/$CoFe_2O_4$@NC	280 @ 10	49.7	50 h at 10 mA cm^{-2}	29
$Fe_2O_3/Fe_{0.64}Ni_{0.36}$@Cs	274 @ 10	82.9	15 h at 10 mA cm^{-2}	30
NiHCF	330 @ 10	73	35000 s at 10 mA cm^{-2}	31
Fe-CoO/Co	276 @ 10	57	57 h at 10 mA cm^{-2}	32
$Ni_{40}Fe_{40}B_{20}$	319 @ 10	56	24 h at 100 mA cm^{-2}	33
$NiFeWO_4$-3	235 @ 10	42	110 h at 290 mA cm^{-2}	This work

Table S2. Comparison of overall water splitting performances at 10 mA cm^{-2} with recently-reported catalysts.

Electrocatalyst	Overpotentail / mV@ (10 mA cm^{-2})	References
Pt/C ‖ $Mo_{50}Ni_{41}Fe_9$	1.56	34
D_2-Ni_3S_2//D_2-Ni_3S_2	1.52	35
NiWC-2/CNFs‖NiWC-2/CNFs	1.55	36
$NiSe_2$–$CoSe_2$ ‖ $NiSe_2$–$CoSe_2$	1.63	37
CoFe10%-P/NF ‖ CoFe10%-P/NF	1.63	38
Pt/C ‖ a/c-NiFeMoO$_x$	1.52	39
Fe_4Co_6@NDC/NF ‖ PtC/NF	1.57	40
Fe-MoS ‖ NiS@NF	1.60	41
IL-Fe-SAC-8 ‖ IL-Fe-SAC-8	1.58	42
CoCuFeNiMnMo$_{1.5}$ ‖ CoCuFeNiMnMo$_{0.5}$	1.76 V	43

Fe-MoS/NiS@NF ∥ Fe-MoS/NiS@NF	1.60	44
FeCoNi ∥ FeCoNi	1.62	45
NF@G-5@Ni_3S_2 ∥ NF@G-5@Ni_3S_2	1.62	40
$Cr_{0.05}Ni_{0.95}Se_2$ ∥ $Cr_{0.05}Ni_{0.95}Se_2$	1.58	46
Ru/Mo_2C ∥ Ru/Mo_2C	1.51	47
$CoCuFeNiMnMo_{1.5}$ ∥ $CoCuFeNiMnMo_{1.5}$	1.76	43
Pt/C ∥ RuO_2	1.56	This work
Pt/C ∥ $NiFeWO_4$-3	1.48	This work

References

1 Z. W. Liu, Q. C. Zhang, L. X. Wen, J. F. Chen, *Can. J. Chem. Eng.,* 2016, **94**, 461-468.

2 G. Kresse, J. Furthmüller, *Phys. Rev. B*, 1996, **54**, 11169-11186.

3 S. Grimme, J. Antony, S. Ehrlich, H. Krieg, *J. Chem. Phys*., 2010, **132**, 154104.

4 K. Mathew, R. Sundararaman, K. Letchworth-Weaver, T. A. Arias, R. G. Hennig, *J. Chem. Phys*., 2014, **140**, 084106.

5 G. Kresse, D. Joubert, *Phys. Rev. B*, 1999, **59**, 1758.

6 J. P. Perdew, K. Burke, M. Ernzerhof, *Phys. Rev. Lett*., 1996, **77**, 3865-3868.

7 A. Kuzmin, A. Kalinko, R. Evarestov, *Open Phys*., 2011, **9**, 502-509.

8 B. Walls, A. A. Mazilkin, B. O. Mukhamedov, A. Ionov, I. A. Smirnova, A. V. Ponomareva, K. Fleischer, N. A. Kozlovskaya, D. A. Shulyatev, I. A. Abrikosov, I. V. Shvets, S. I. Bozhko, *Sci. Rep*., 2021, **11**, 3496.

9 N. Doudin, S. Pomp, M. Blatnik, R. Resel, M. Vorokhta, J. Goniakowski, C. Noguera, F. P. Netzer, S. Surnev, *Surf Sci*., 2017, **659**, 20-30.

10 R. Poulain, A. Klein, J. Proost, *J. Phys. Chem. C*., 2018, **122**, 22252-22263.

11 S. Sakong, M. Naderian, K. Mathew, R. G. Hennig, A. Groß, *J. Chem. Phys*., 2015, **142**, 234107.

12 Z. Liu, L. Guo, T. Huang, L. Wen, J. Chen, *Chem. Eng. Sci.,* 2014, **119**, 124-133.

13 X. Zhang, P. Tan, H. Liao, Y. Zhang, X. Liu, M. Zhang, H. Huang, J. Pan, *J. Electroanal. Chem.,* 2023, **940**, 117454.

14 N. Mironova-Ulmane, A. Kuzmin, I. Steins, J. Grabis, I. Sildos, M. Pärs, *J. Electroanal. Chem*., 2007, **93**, 012039

15 M.-L. Lu, T.-Y. Lin, T.-M. Weng, Y.-F. Chen, *Optics express*., 2011, **19 (17)**, 16266-16272.

16 P. Bagwade, D. Malavekar, S. Ubale, R. Bulakhe, I. In, U. Patil, C. Lokhande, *Electrochimica Acta*., 2022, **408**, 139933.

17 M. Kassaee, E. Motamedi, M. Majdi, *Chem. Eng. J*., 2011, **172 (1)**, 540-549.

18 M. Aliahmad, M. Noori, *Indian J. Phys.,* 2013, **87**, 431-434.

19 P.-F. Guo, Y. Yang, W.-J. Wang, B. Zhu, W.-T. Wang, Z.-Y. Wang, J.-L. Wang, K. Wang, Z.-H. He, Z.-T. Liu, *Chem. Eng. J*., 2021, **426**.

20 J. Zhang, M. Zhang, L. Qiu, Y. Zeng, J. Chen, C. Zhu, Y. Yu, Z. Zhu, *J. Mater. Chem. A*, 2019, **7**, 19045-19059.

21 L. Zhang, W. Cai, N. Bao, *Adv Mater*, 2021, **33**, e2100745.

22 X. Hou, H. Zhou, M. Zhao, Y. Cai, Q. Wei, *ACS Sustainable Chem. Eng*., 2020, **8**, 5724-5733.

23 S. Liu, R. Wan, Z. Lin, Z. Liu, Y. Liu, Y. Tian, D.-D. Qin, Z. Tang, *J. Mater. Chem*., 2022, **10**, 5244-5254.

24 S. Yue, S. Wang, Q. Jiao, X. Feng, K. Zhan, Y. Dai, C. Feng, H. Li, T. Feng, Y. Zhao, *ChemSusChem*, 2019, **12**, 4461-4470.

25 Q. Wang, J. Li, Y. Li, G. Shao, Z. Jia, B. Shen, *Nano Res*., 2022, **15**, 8751-8759.

26 X. Li, H. Zhang, Q. Hu, W. Zhou, J. Shao, X. Jiang, C. Feng, H. Yang, C. He, *Angew. Chem. Int. Ed*., 2023, **62**, e202300478.

27 K. Zeng, Y. Li, M. Tian, C. Wei, J. Yan, M. H. Rummeli, P. Strasser, R. Yang, *Energy Storage Mater*., 2023, **60**, 102806.

28 V. Ananth, V. Ashok, S. Mathi, S. Pandiaraj, S. Rahman, N. Alarifi, A. N. Alodhayb, N. P. Shetti, *Flatchem*, 2024, **45**,100648.

29 Y.-G. Ji, J. Wu, H. Wen, S. Wang, L. Feng, *Chem. Eng. J*., 2024, **496**, 154211.

30 F. Zhou, M. Gan, D. Yan, X. Chen, X. Peng, *Small*, 2023, **19**, 2208276.

31 M. Khairy, K. G. Mahmoud, H. M. El-Sagher, *Int. J. Hydrogen Energy*, 2023, **48**, 29887-29897.

32 S. M. Liu, Y. P. Yang, M. L. Zhong, S. C. Li, S. L. Shi, W. M. Xiao, S. H. Wang, C. Chen, *Dalton Trans*., 2023, **52**, 15928-15934.

33 H. L. Li, Y. Y. Wang, C. M. Liu, S. M. Zhang, H. F. Zhang, Z. W. Zhu, *Int. J. Hydrogen Energy*, 2022, **47**, 20718-20728.

34 X. L. Luo, Q. Shao, Y. C. Pi, X. Q. Huang, *ACS Catal*., 2019, **9**, 1013-1018.

35 F. T. Luo, Y. Liu, X. Jiang, J. Fan, S. J. Chen, *Appl. Phys. Lett*., 2023, **122**.

36 S. G. Zhang, G. H. Gao, H. Zhu, L. J. Cai, X. D. Jiang, S. L. Lu, F. Duan, W. F. Dong, Y. Chai, M. L. Du, *Sci. Bull*., 2020, **65**, 640-650.

37 H. C. Liu, F. Yang, F. J. Chen, S. Che, N. Chen, C. Xu, N. Wu, W. K. Wei, Y. F. Li, *Mater. Chem. Front*., 2023, **7**, 1365-1373.

38 B. H. Liu, S. Y. Li, T. Q. Wang, Y. Yang, L. X. Wang, X. Zhang, Z. C. Liu, L. W. Niu, *Catal. Commun*., 2023, **175**, 106607.

39 K. Zeng, Y. B. Li, M. Tian, C. H. Wei, J. Yan, M. H. Rummeli, P. Strasser, R. Z. Yang, *Energy Storage Mater.,* 2023, **60**, 102806.

40 C. Jin, N. Zhou, Y. Wang, X. Li, M. Chen, Y. Dong, Z. Yu, Y. Liang, D. Qu, Y. Dong, Z. Xie, C. Zhang, *J. Electroanal. Chem.*, 2020, **858**, 13795.

41 T. Wang, B. W. Li, P. Wang, M. Xu, D. D. Wang, Y. Q. Wang, W. J. Zhang, C. Q. Qu, M. Feng, *J. Colloid Interface Sci*., 2024, **672**, 715-723.

42 A. Sathyaseelan, V. Elumalai, M. Perumalsamy, N. Ul Haq Liyakath Ali, A. Sajeev, S.-J. Kim, *Chem. Eng. J*., 2024, **489**, 151235.

43 Asghari Alamdari, H. Jahangiri, M. B. Yagci, K. Igarashi, H. Matsumoto, A. Motallebzadeh, U. Unal, *Applied Energy Materials*, 2024, **7**, 2423-2435.

44 T. Wang, B. Li, P. Wang, M. Xu, D. Wang, Y. Wang, W. Zhang, C. Qu, M. Feng, *J. Colloid Interface Sci*., 2024, **672**, 715-723.

45 Y. W. Chen, L. X. Yang, C. Li, Y. Q. Wu, X. Lv, H. R. Wang, J. E. Qu, *Energy Environ. Mater*., 2024, **7**, e12590.

46 H. Fan, D. Jiao, J. Fan, D. Wang, B. Zaman, W. Zhang, L. Zhang, W. Zheng, X. Cui, *Nano Res*., 2024, **17**, 1199-208.

47 Z. Liu, Y. Liu, H. He, H. Shao, Y. Zhang, J. Li, W. Cai, *Electrochim. Acta*, 2023, **443**, 41920.